

# Stable Eutectoid Transformation in Nodular Cast Iron: Modeling and Validation



FERNANDO D. CARAZO, PATRICIA M. DARDATI, DIEGO J. CELENTANO,  
and LUIS A. GODOY

This paper presents a new microstructural model of the stable eutectoid transformation in a spheroidal cast iron. The model takes into account the nucleation and growth of ferrite grains and the growth of graphite spheroids. Different laws are assumed for the growth of both phases during and below the intercritical stable eutectoid. At a microstructural level, the initial conditions for the phase transformations are obtained from the microstructural simulation of solidification of the material, which considers the divorced eutectic and the subsequent growth of graphite spheroids up to the initiation of the stable eutectoid transformation. The temperature field is obtained by solving the energy equation by means of finite elements. The microstructural (phase change) and macrostructural (energy balance) models are coupled by a sequential multiscale procedure. Experimental validation of the model is achieved by comparison with measured values of fractions and radius of 2D view of ferrite grains. Agreement with such experiments indicates that the present model is capable of predicting ferrite phase fraction and grain size with reasonable accuracy.

DOI: 10.1007/s11661-016-3827-6

© The Minerals, Metals & Materials Society and ASM International 2016

## I. INTRODUCTION

CAST irons are Fe-C-Si alloys in which graphite, ferrite, and pearlite are the microconstituents at ambient temperature. Ferrite is a solid solution of carbon in BCC iron, cementite is the chemical compound  $\text{Fe}_3\text{C}$ , and pearlite is a laminar microconstituent formed by ferrite and cementite. The mechanical properties of cast irons largely depend on their microstructure, *i.e.*, type, fractions, size, and size distribution of its microconstituents.<sup>[1,2]</sup>

Nucleation and growth processes of graphite are of great importance in predicting the final graphite fraction and quantity and size distribution of graphite spheroids, and this greatly influences the final mechanical properties of the alloy at ambient temperature.<sup>[3]</sup> Regarding ferrite, a common assumption is that graphite spheroids are surrounded

by ferrite shells. To illustrate the nature of ferrite, the micrograph in Figure 1 shows that shells are formed by large ferrite grains without a texture, which in most cases completely surround the spheroids. However, depending on the composition of the alloy and the cooling characteristics of the process, the spheroids may be partially covered by ferrite or even have no ferrite on their surface.

Testing is of course the main source of information with regard to the cooling process and transformations that take place in a cast iron part. However, there are cost limitations and also difficulties in visualizing all parts of a process without causing interference with the same process which is being observed. This has motivated a growing interest in modeling the thermal and metallurgical process by means of computational mechanics. The successful application of such models largely depends on qualitative as well as quantitative aspects, *i.e.*, a correct understanding of the nature of the process under consideration, and an accurate evaluation of parameters and variables involved.

Considerable progress has been made in modeling solid state transformations in nodular cast iron during the last two decades, but there are still many limitations in current modeling capabilities. Such limitations include the prediction of ferrite grain size and quantity, together with its influence on the growth of graphite spheroids. Other unexplored areas include the influence of ferrite on the possibility that a metastable eutectoid transformation occurs while the temperature of alloy is still in the intercritical stable eutectoid range, causing a competitive situation between the stable and metastable eutectoid phase changes.

This paper addresses some of the limitations described above by means of a new computational thermo-metallurgical model of stable eutectoid phase change of

---

FERNANDO D. CARAZO, Professor and Researcher, is with Instituto de Mecánica Aplicada, Universidad Nacional de San Juan, Av. Libertador Gral. San Martín 1109 (Oeste), C.P. J5400ARL, San Juan, Argentina, and also with CONICET, C1425FQB, Godoy Cruz 2290, C.A.B.A., Argentina. Contact e-mail: fcarazo@unsj.edu.ar  
PATRICIA M. DARDATI, Professor, is with GIDMA and Departamento de Ingeniería Mecánica, Universidad Tecnológica Nacional Facultad Regional Córdoba, Maestro M. López esq. Cruz Roja Argentina s/n, Ciudad Universitaria, Córdoba, Argentina. DIEGO J. CELENTANO, Professor, is with Departamento de Ingeniería Mecánica y Metalúrgica, Research Center for Nanotechnology and Advanced Materials (CIEN-UC), Pontificia Universidad Católica de Chile, Av. Vicuña Mackenna 4860, Macul, Santiago, Chile. LUIS A. GODOY, Plenary Professor, is with the Institute for Advanced Studies in Engineering and Technology, FCEfyN, National University of Córdoba and CONICET, Av. Vélez Sarsfield 1601, Córdoba, Argentina, and also with CONICET, C1425FQB, Godoy Cruz 2290, C.A.B.A., Argentina.

Manuscript submitted March 16, 2016.

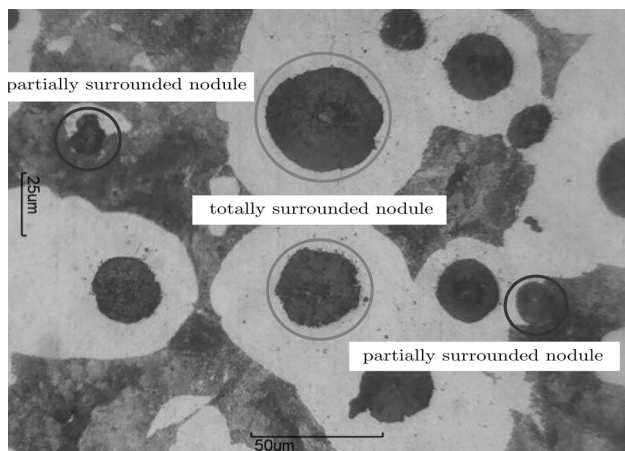


Fig. 1—Illustration of spheroids which are fully or partially surrounded by ferrite (400 times).

spheroidal cast irons. The model aims to improve current understanding and design of isothermal heat treatments, or heat treatments with continuous cooling, for which the temperature is kept at the intercritical stable eutectoid range.<sup>[4]</sup>

## II. LITERATURE REVIEW

To the best of our knowledge, there are few contributions to the technical literature review in which the coupling of a macrostructural model of cooling of spheroidal cast irons with solidification and stable and metastable eutectoid transformations.<sup>[5–9]</sup> This modeling capability is important to account for the main microstructural features of the solidification process and subsequent cooling on the stable and metastable eutectoid phase changes, *i.e.*, considering the divorced eutectic and growth of graphite spheroids from the end of solidification up to the upper limit of intercritical stable eutectoid. The importance of this coupling emerges from the need to include the inherited characteristics of solidification into the phase changes in solid state, because this may modify the way in which subsequent phase changes occur, or even become an obstacle to their development.

In the work of Stefanescu and Kanetkar,<sup>[5]</sup> a given number of ferrite nuclei is assumed at the beginning of the process. The growth of ferrite is computed from carbon diffusion through ferrite toward the graphite spheroids.

Liu *et al.*<sup>[6]</sup> assumed that ferrite envelopes nucleate instantaneously on the spheroids and considered the carbon diffusion toward spheroidal graphite from eutectic austenite to evaluate the growth rate of these envelopes.

Chang *et al.*<sup>[7]</sup> studied stable and metastable eutectoid transformations as two processes that compete for the carbon that diffuses from austenite. The spheroids are assumed to be surrounded by ferrite when the stable eutectoid temperature is reached. As ferrite grows, it forms an envelope on graphite spheroids. Finally, the growth

of graphite spheroids is assumed to be caused by carbon diffusion through ferrite.

The influence of Si microsegregation on the equilibrium carbon concentrations and the temperatures of the stable and metastable eutectoid transformations have been considered by Almansour *et al.*<sup>[8]</sup> Once again, the eutectoid transformation is taken as a competitive growth process between stable and metastable eutectoid phase changes. Although these authors coupled the stable eutectoid transformation in a microstructural solidification model, the growth of ferrite shells is limited to a critical size that depends on silicon microsegregation.

Wessen and Svensson<sup>[9]</sup> presented a model of stable eutectoid transformation of an eutectic nodular cast iron in which stable and metastable eutectoid transformations are viewed as two competitive processes. It is assumed that the growth of ferrite stops when the metastable eutectoid temperature is reached. Based on experimental observations, the model considers that four ferrite grains nucleate on each graphite spheroid when the temperature in the alloy reaches 1063 K (790 °C). In this work, the growth of ferrite is divided into three stages. In the first stage, the differences in carbon concentrations at equilibrium in ferrite at the interphase with austenite and with graphite are assumed to be small, and, therefore, the driving force for carbon to diffuse through ferrite is also small. Thus, the growth of ferrite depends on the carbon diffusion from austenite to zones of austenite that are located away from the interface with ferrite. Once the graphite spheroids are completely surrounded by ferrite, the growth of ferrite grains is considered as a function of carbon diffusion toward graphite spheroids. In this second stage, the authors consider that the mechanism controlling diffusion is of an interfacial nature. In the third stage, the authors assumed that, as the thickness of the ferrite shell increases, the flow of carbon through ferrite is the mechanism controlling the growth rate of the process.

A model for the phase transformation in solid state of a spheroidal cast iron was presented by Lacaze and Gerval.<sup>[10]</sup> The authors state that stable and metastable eutectoid transformations are two competitive processes, but the growth of ferrite stops when the alloy reaches the upper bound of intercritical metastable eutectoid range. In this model, the nucleation of ferrite grains is not represented and, as the stable eutectoid temperature is reached, it is assumed that each graphite spheroid is surrounded by a ferrite shell with 0.1 µm thickness. The growth of the ferrite shell is modeled by carbon diffusion toward graphite spheroids and toward austenite located away from the interface with ferrite, considering that the flow of carbon by which austenite transforms into ferrite initially occurs by an interfacial reaction between ferrite and graphite, whereas carbon diffusion occurs through ferrite and austenite in a second stage. The growth of graphite spheroids was computed as a function of carbon flow from austenite at the interface with ferrite to the graphite spheroids through the ferrite shells.

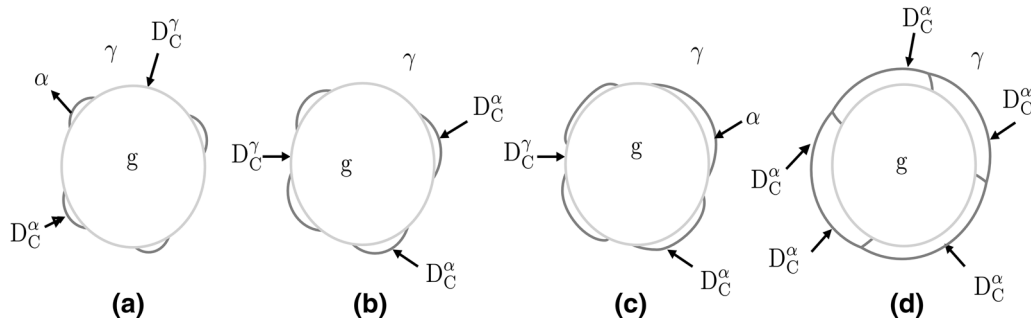


Fig. 2—Schematic representation of nucleation and growth of ferrite grains of a nodular cast iron. (a) Nucleation of ferrite grains for  $A_{\alpha/g} \approx 0$ . (b) Growth of ferrite grains for  $A_{\alpha/g} \leq A_{\gamma/g}$ . (c) Growth of ferrite grains for  $A_{\alpha/g} \geq A_{\gamma/g}$ . (d) Growth of ferrite grains for  $A_{\alpha/g} \approx 1$ .

In the model discussed by Venugopalan,<sup>[11]</sup> the incubation time is considered for nucleation of ferrite envelope on each graphite spheroid. Carbon diffusion through ferrite is taken into account to evaluate the fraction of austenite transformed. An important feature of this work is the influence of the alloy components on the carbon diffusion coefficient through ferrite. The same author developed a model of stable eutectoid transformation which was applied to isothermal treatments.<sup>[12]</sup> The nucleation of ferrite grains is not considered in References 11, 12; instead, an incubation time is assumed for the ferrite envelope to form on the spheroids. Further, the model includes that carbon diffusion through ferrite and austenite contribute to the growth of a ferrite shell and thus to the growth of the spheroids.

In Reference 13, the authors considered that nodules are surrounded by ferrite when the stable eutectoid temperature is reached. The growth of nodules is due to the carbon diffusion from ferrite to graphite, and the growth of ferrite envelopes are due to carbon diffusion from austenite to the same phase away the interphase with ferrite and from ferrite at the interphase with austenite and the nodules. The main differences with the present model to be presented in this work is that the system used in the solid state transformation is binary, *i.e.*, the upper and lower bounds of intercriticals stable and metastable eutectoid ranges are not considered, the laws of ferrite growth are the same during the intercritical stable eutectoid and below the lower bound of this range, and it does not differentiate the diffusion of carbon from ferrite or austenite to graphite in nodules growth rate.

The literature review shows that several features cannot be clearly explained at present, including the forming process of ausferrite,<sup>[4]</sup> and the presence of spheroids that are not fully enclosed by the ferrite grains, as shown in Figure 1. These are the main aspects that motivated the development of the present work. The model including these phenomena is described in Section III, while its application is presented in Section IV. The experimental validation of the corresponding numerical results is discussed in Section V. Finally, the conclusions drawn from this study are presented in Section VI.

### III. MODEL FOR THE STABLE EUTECTOID TRANSFORMATION

In the model proposed in this work, the stable eutectoid transformation is assumed to occur in two stages, as shown in Figure 2: first, the nucleation of ferrite grains and second, the growth of graphite spheroids and ferrite grains under various conditions. The latter stage includes the growth that occurs at the intercritical stable eutectoid, and the growth that occurs at temperatures lower than the lower bound of the intercritical stable eutectoid, shown in Figure 3. Each stage is discussed in detail in the following sections.

#### A. Nucleation of Ferrite Grains

As proposed by Wessen and Svensson,<sup>[9]</sup> nucleation of ferrite grains is modeled as an instantaneous process by assuming that a given number of ferrite grains nucleate on each graphite spheroid when the alloy temperature reaches the upper bound of the intercritical stable eutectoid range ( $T_{\alpha\gamma}^z$ ); see Figure 2(a).

#### B. Growth of Ferrite Grains and Graphite Spheroids During the Intercritical Stable Eutectoid

Whenever the temperature is between the upper and lower bounds of an intercritical stable eutectoid range, respectively, denoted as  $T_{\alpha\gamma}^z$  and  $T_{\alpha\gamma}^x$  in Figures 3(a) and (b), carbon diffusion may be due to

- The difference between carbon concentration in austenite ( $C_C^{\gamma}$ ) and carbon concentration at equilibrium in austenite in contact with graphite ( $C_C^{\gamma/g}$ ).
- The difference between  $C_C^{\gamma}$  and carbon concentration at equilibrium in austenite in contact with ferrite ( $C_C^{\gamma/\alpha}$ ); see Figure 4.

Values of intercritical stable eutectoid bounds and the expressions for the evaluation of carbon concentration at equilibrium employed in the laws of growth of ferrite grains and graphite spheroids are defined in Appendix A.

##### 1. Growth of ferrite grains

The growth of ferrite grains during the intercritical stable eutectoid is due to carbon diffusion from austenite

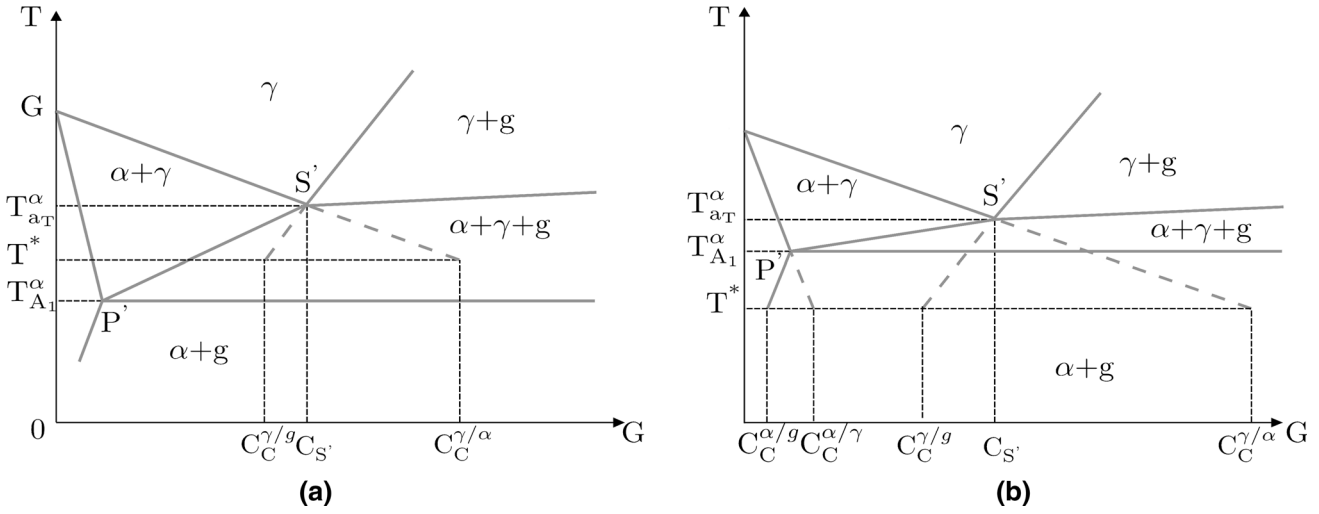


Fig. 3—Schematic of an isopleth Fe-C section of the Fe-C-Si equilibrium phase diagram with the indication of stable and metastable equilibrium carbon concentrations (solid and broken lines, respectively) for: (a) A temperature between the upper and lower bounds of the intercritical stable eutectoid range, (b) a temperature lower than the lower bound of the intercritical stable eutectoid range (Reprinted from Ref. [17]).

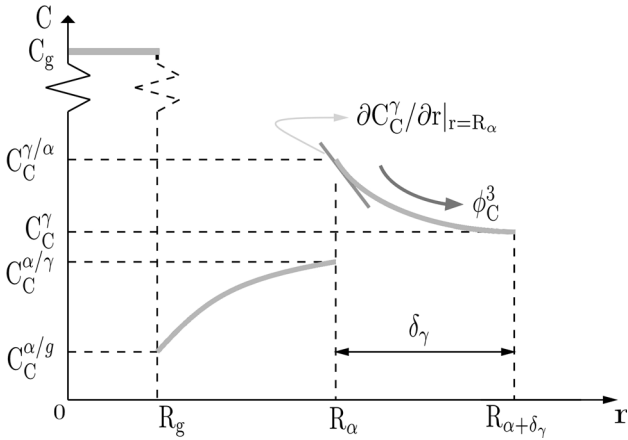


Fig. 4—Indication of carbon gradient that gives rise to  $\phi_C^3$  during intercritical stable eutectoid.

in contact with ferrite toward austenite located away from the interface with ferrite. The value of carbon flow  $\phi_C^3$  plotted in Figure 4 results from the first Fick law:<sup>[14]</sup>

$$\phi_C^3 = -\rho_\gamma D_C^\gamma \left. \frac{\partial C_C^\gamma}{\partial r} \right|_{r=R_x}, \quad [1]$$

where  $D_C^\gamma$  is the diffusion coefficient of carbon in austenite,  $\rho_\gamma$  is the density of austenite, and  $\left. \frac{\partial C_C^\gamma}{\partial r} \right|_{r=R_x}$  is the gradient of carbon concentration in austenite at the interface with ferrite. Carbon that diffuses from austenite at the interface with ferrite to the austenite far from ferrite is incorporated into the latter as

$$\phi_C^3 = (\rho_\gamma C_C^{\gamma/\alpha} - \rho_\alpha C_C^{\alpha/\gamma}) \dot{R}_x, \quad [2]$$

where  $\dot{R}_x$  is the rate of change of ferrite grain radius (*i.e.*, the rate at which the ferrite/austenite interface advances toward austenite),  $\rho_\alpha$  is the density of ferrite, and  $C_C^{\gamma/\alpha}$  is the equilibrium carbon concentration in ferrite in contact with austenite. From Eqs. [1] and [2], one gets

$$\dot{R}_x = -D_C^\gamma \rho_\gamma \frac{1}{\left( C_C^{\gamma/\alpha} - \rho_\alpha / \rho_\gamma C_C^{\alpha/\gamma} \right)} \left. \frac{\partial C_C^\gamma}{\partial r} \right|_{r=R_x}, \quad [3]$$

where  $\left. \frac{\partial C_C^\gamma}{\partial r} \right|_{r=R_x}$  is the only unknown in the right-hand side of Eq. [3] whose evaluation requires knowledge of the profile shape of carbon concentration through the austenite. Considering that the rate of carbon diffusion from the austenite at the interface with ferrite to the austenite far from ferrite is higher than the rate of advance of the ferrite, it is possible to assume that carbon diffusion is a quasi-stationary process. Thus, according to Shewmon,<sup>[15]</sup> the gradient of carbon for a quasi-stationary solute profile with the boundary conditions on the spheroid shown in Figure 4 is

$$\left. \frac{\partial C_C^\gamma}{\partial r} \right|_{r=R_x} = \left( C_C^\gamma - C_C^{\gamma/\alpha} \right) \frac{(R_x - \delta_\gamma)}{\delta_\gamma R_x}, \quad [4]$$

where  $R_x$  is ferrite grain radius and  $\delta_\gamma$  is the austenite boundary layer in front of the ferrite grains. The value of  $\delta_\gamma$  is calculated by taking into account the same considerations as those by Kurz and Fisher.<sup>[16]</sup>

Substituting Eqs. [4] into [3], the growth rate of the ferrite grain radius during the intercritical stable eutectoid is given by:

$$\dot{R}_x = D_C^\gamma \frac{\left( C_C^{\gamma/\alpha} - C_C^\gamma \right)}{\left( C_C^{\gamma/\alpha} - \rho_\alpha / \rho_\gamma C_C^{\alpha/\gamma} \right)} \frac{(R_x + \delta_\gamma)}{R_x \delta_\gamma}. \quad [5]$$



Regarding the growth of ferrite during the intercritical stable eutectoid, three points should be taken into account: (i) The growth of ferrite grains takes place if and only if  $(C_C^{\gamma/\alpha} - C_C^{\gamma}) > 0$ ; this inequality may or may not be satisfied, because in the present model the value of  $C_C^{\gamma}$  results from mass conservation of carbon in a characteristic volume element (Eq. [B1] in Appendix B). (ii) From a phenomenological point of view, the growth of ferrite grains in this stage is very important because it causes a carbon enrichment in austenite located away from ferrite that may produce the formation of either carbides or pearlite that nucleates from enriched austenite that became unstable for temperatures higher than the lower bound of the intercritical metastable eutectoid. (iii) From the model presented in this section, it is possible to explain the growth of ferrite grains during isothermal heat treatments at temperatures between the upper and lower bound of the intercritical stable eutectoid during which ferrite grows to the expense of carbon that diffuses toward austenite away from ferrite,<sup>[4]</sup> and without a growth of graphite spheroids or the nucleation of pearlite colonies which may form pearlite grains or nodules.

## 2. Growth of graphite spheroids

Following nucleation of ferrite grains, graphite spheroids should be fully or partially covered depending on the size of spheroids and the number and size of ferrite grains at the nucleation, as shown in Figure 2. For temperatures within the intercritical stable eutectoid, the condition  $(C_C^{\alpha/\gamma} - C_C^{\alpha/g}) < 0$  is satisfied. This may be observed in Figure 3(a) by extrapolation of the line of  $C_C^{\alpha/g}$  for temperatures higher than the lower bound of intercritical stable eutectoid.

This indicates that, even if a graphite/ferrite interface had been created during the intercritical stable eutectoid, the growth of graphite spheroids depends on carbon diffusion from austenite at the interface with graphite to graphite, and not through the surface occupied by ferrite. Following the procedure employed in Reference 17, then:

$$\dot{R}_g = \frac{D_C^\gamma}{R_g} \frac{(C_C^\gamma - C_C^{\gamma/g})}{(\rho_g/\rho_\gamma C_g - C_C^{\gamma/g})} A_{\gamma/g}, \quad [6]$$

where  $\rho_g$  and  $C_g$  are density and carbon content in graphite,  $A_{\gamma/g}$  is a coefficient that takes into account the fraction of the nodules surface in contact with austenite, *i.e.*,  $0 \leq A_{\gamma/g} \leq 1$ , such that  $A_{\gamma/g} = 1$  for the start of the transformation, while  $A_{\gamma/g} = 0$  is achieved when the spheroid is completely covered by ferrite grains;  $A_{\gamma/g}$  is calculated as proposed in Eq. [B2] in Appendix B. In Eq. [6], a spheroid that is fully covered by ferrite (*i.e.*,  $A_{\gamma/g} = 0$ ) means that it is not in contact with austenite, and this implies that there is no carbon diffusion from such phase to the graphite spheroids. The value of  $C_C^{\gamma/g}$  in Eq. [6] is obtained by extrapolation of the line of maximum solubility of carbon in austenite for

temperatures lower than  $T_{Ar}^\alpha$ , depending on the values of Si concentration in austenite ( $C_{Si}$ ) in contact with graphite or in the first zone of solidification. A detailed explanation of the derivation of Eq. [6] may be found in Reference 17.

The importance of the size of a spheroid on the growth of graphite and ferrite during the intercritical stable eutectoid is highlighted in this model. For a given initial number and size of ferrite grains nucleated on a spheroid, the value of  $A_{\gamma/g}$  in Eq. [6] approaches 1 as the dimensions of the spheroid become larger. This directly contributes to the growth of graphite spheroids and to the carbon decrease in the austenite that surrounds the spheroids, which in turn favors the transformation of austenite into ferrite at the interface with graphite and with ferrite. Further, there is an increase in the size of spheroids, with  $D_C^\alpha$  (diffusion coefficient of carbon in ferrite) being approximately 100 times larger than  $D_C^\gamma$ . This process stimulates the formation of ferrite grains on the spheroids.

## C. Growth of Ferrite Grains and Graphite Spheroids at Temperatures Lower Than the Lower Bound of the Intercritical Stable Eutectoid

Once ferrite grains completely surround the graphite spheroids, then carbon flow due to the carbon concentration gradient in ferrite in contact with graphite, identified as  $\phi_C^2$  in Figure 5, pushes carbon toward the spheroids through ferrite. Moreover, the carbon flow caused by the carbon concentration gradient in austenite in contact with ferrite, identified as  $\phi_C^3$  in Figure 5, continues pushing carbon toward austenite located away from the interface with ferrite; this causes an impoverishment of carbon in austenite in contact with ferrite and the growth of ferrite grains. As the temperature decreases, the value of  $\phi_C^2$  also decrease due to an increase in the thickness of the ferrite shell. In the final stages of growth of ferrite grains, the value of  $C_C^\gamma$  decreases because austenite loses carbon with a decrease in temperature, and the shell thickness of ferrite grains

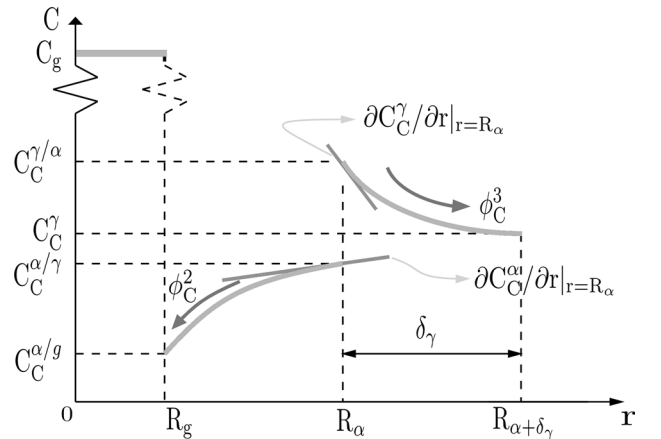


Fig. 5—Indication of carbon concentration gradients that gives rise  $\phi_C^2$  and  $\phi_C^3$  at temperatures below  $T_{Ar}^\alpha$ .

and  $C_C^{\gamma/\alpha}$  increase, as indicated in Figures 4 and 3(a), respectively. Thus, carbon diffusion toward austenite located away from ferrite controls the growth of ferrite grains.

When the alloy temperature becomes lower than  $T_{A_1}^\alpha$  shown in Figure 3(b), the driving forces for carbon diffusion become:

- The differences between  $C_C^{\gamma/\alpha}$  and  $C_C^\gamma$ , shown in Figures 4 and 5.
- The differences between  $C_C^{\alpha/\gamma}$  and  $C_C^{\alpha/g}$ , shown in Figure 5.
- The differences between  $C_C^\gamma$  and  $C_C^{\gamma/g}$ .

Notice that the growth of graphite spheroids depends on carbon diffusion through ferrite if  $A_{\gamma/g} = 0$ , whereas the diffusion occurs through ferrite and austenite if  $A_{\gamma/g} \neq 0$ .

### 1. Growth of ferrite grains

On the basis of the explanations given in Section III-C, then the carbon flow which causes a growth of ferrite grains may be quantified as

$$\phi_C^2 + \phi_C^3 = -\rho_\alpha D_C^\alpha \frac{\partial C_C^\alpha}{\partial r} \Big|_{r=R_\alpha} - \rho_\gamma D_C^\gamma \frac{\partial C_C^\gamma}{\partial r} \Big|_{r=R_\alpha}, \quad [7]$$

where  $\partial C_C^\alpha / \partial r \Big|_{r=R_\alpha}$  is the gradient of carbon concentration in ferrite in contact with austenite. Carbon diffusion toward the graphite spheroids and toward austenite away from ferrite is compensated by the advance of ferrite grains. Thus, the condition:

$$\phi_C^2 + \phi_C^3 = \rho_\alpha \left( C_C^{\gamma/\alpha} - C_C^{\alpha/\gamma} \right) \dot{R}_\alpha \quad [8]$$

must be satisfied. Equilibrium of carbon in ferrite at the interface with austenite requires that Eqs. [7] and [8] should be equated. Thus, the growth rate of ferrite grains should be

$$\dot{R}_\alpha = D_C^\alpha \frac{1}{\left( C_C^{\gamma/\alpha} - C_C^{\alpha/\gamma} \right)} \frac{\partial C_C^\alpha}{\partial r} \Big|_{r=R_\alpha} + D_C^\gamma \frac{\rho_\gamma}{\rho_\alpha} \frac{1}{\left( C_C^{\gamma/\alpha} - C_C^{\alpha/\gamma} \right)} \frac{\partial C_C^\gamma}{\partial r} \Big|_{r=R_\alpha}. \quad [9]$$

With the values of carbon concentration at the interfaces of ferrite and austenite shown in Figure 5, the carbon gradients included in Eq. [9] also shown in Figure 5 and are given by:

$$\begin{aligned} \frac{\partial C_C^\alpha}{\partial r} \Big|_{r=R_\alpha} &= \frac{\left( C_C^{\alpha/\gamma} - C_C^{\alpha/g} \right) R_g}{R_\alpha (R_\alpha - R_g)}, \\ \frac{\partial C_C^\gamma}{\partial r} \Big|_{r=R_\alpha} &= \left( C_C^\gamma - C_C^{\gamma/\alpha} \right) \frac{R_\alpha + \delta_\gamma}{\delta_\gamma R_\alpha}. \end{aligned} \quad [10]$$

Substitution of Eq. [10] into [9], it leads to the following growth rate of ferrite grains:

$$\begin{aligned} \dot{R}_\alpha &= D_C^\alpha \frac{\left( C_C^{\alpha/\gamma} - C_C^{\alpha/g} \right)}{\left( C_C^{\gamma/\alpha} - C_C^{\alpha/\gamma} \right)} \frac{R_g}{R_\alpha (R_\alpha - R_g)} + \\ &D_C^\gamma \frac{\rho_\gamma}{\rho_\alpha} \frac{\left( C_C^{\gamma/\alpha} - C_C^\gamma \right)}{\left( C_C^{\gamma/\alpha} - C_C^{\alpha/\gamma} \right)} \frac{\left( R_\alpha + \delta_\gamma \right)}{\delta_\gamma R_\alpha}. \end{aligned} \quad [11]$$

As assumed in Section III-B-1,  $\phi_C^3$  is zero if  $C_C^\gamma \geq C_C^{\gamma/\alpha}$ .

Once the radius variations of ferrite grains are obtained for an integration time  $\Delta t$ , the radius of a ferrite grain  $i$  at an instant  $t + \Delta t$  ( ${}^{t+\Delta t}R_{\alpha_i}$ ) is

${}^{t+\Delta t}R_{\alpha_i} = {}^tR_{\alpha_i} + \Delta R_{\alpha_i}$ , where  $\Delta R_{\alpha_i}$  is computed by incremental approximation of Eqs. [5] or [11], depending on the alloy temperature and the characteristics of the transformation.

With the radius of ferrite grains, the ferrite volume fraction becomes:

$$f_\alpha = \frac{2}{3} \pi \sum_{i=1}^k N_{g_i}^V n_\alpha (R_{\alpha_i})^3, \text{ where } k \text{ is the number of}$$

events of nucleation of graphite spheroids,  $N_{g_i}^V$  the number of graphite spheroids per unit volume associated with the  $i$  event of nucleation, and  $n_\alpha$  is the number of ferrite grains nucleated on each graphite spheroid.

After transformation of austenite takes place, austenite fraction should be computed again in the form

$$f_\gamma = 1 - f_\alpha - f_g - f_p.$$

Details of the microstructure models from which  $f_g$  and  $f_p$  are calculated are given in Reference 17, 18, respectively.

### 2. Growth of graphite spheroids

In a way similar to the growth of graphite spheroids during the intercritical stable eutectoid, a spheroid that has been fully or partially surrounded by ferrite grains may be in two conditions, as shown in Figures 2(a) through (d). If a spheroid has been fully covered by ferrite grains, as in Figure 2(d), the growth rate of graphite spheroids is given by the condition:

$$\dot{R}_g = D_C^\alpha \frac{\rho_\gamma}{\rho_\alpha} \frac{\left( C_C^{\alpha/\gamma} - C_C^{\alpha/g} \right)}{\left( C_C^g - C_C^{\alpha/g} \right)} \frac{R_\alpha}{R_g (R_\alpha - R_g)}. \quad [12]$$

In case that a graphite spheroid has not been fully covered, as in Figures 2(a) through (c), the growth rate becomes:

$$\dot{R}_g = \dot{R}_g \Big|_{\gamma} A_{\gamma/g} + \dot{R}_g \Big|_{\alpha} A_{\alpha/g}. \quad [13]$$

Terms on the right side of the above equation are computed based on Eqs. [6] and [12]. Further details of Eqs. [12] and [13] may be found in Reference 17.

**Table I. Average Chemical Composition (Main Elements) of the Molten Alloy (Values in Weight Percentage)**

Element	C	Si	Mn	S	P	Cr	Cu	Sn	Mg	CE
Wpt	3.67	2.8	0.21	0.01	0.038	0.025	0.01	0.0009	0.052	4.61

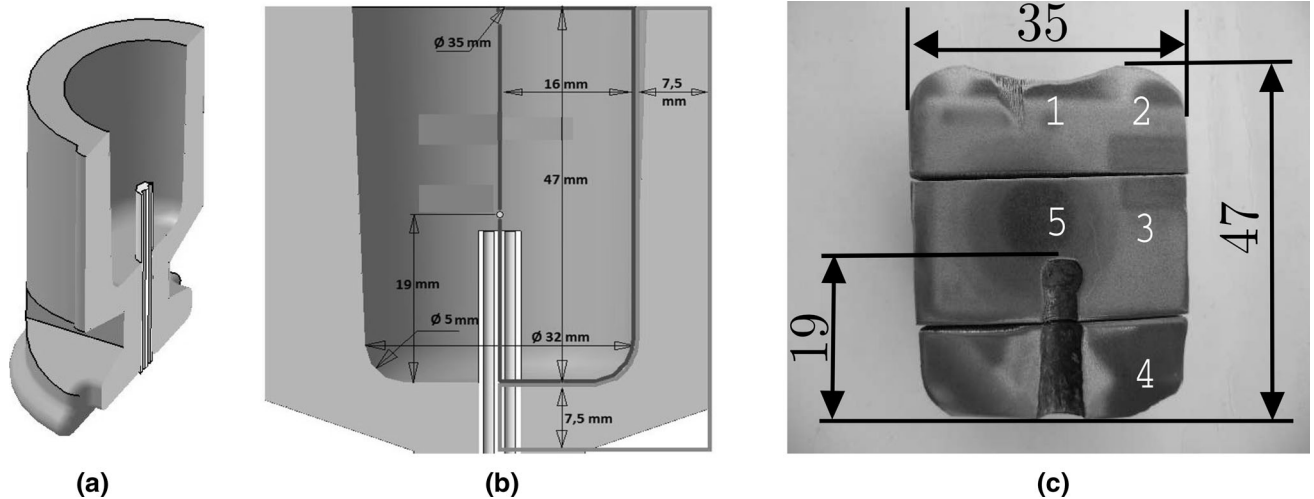


Fig. 6—Sampling cup in which the molten metal was poured. (a) 3D perspective of cup medium. (b) Flat view of cup with the thermocouple, the bifilar, and dimensions. (c) Longitudinal mid-plane section view of the specimen with its dimensions (in mm) and the indication of five microstructurally characterized zones (Reprinted from Ref. [17]).

#### IV. APPLICATION OF THE MODEL

The present model has been applied to the thermo-metallurgical simulation of the cooling of a nodular cast iron with a slightly hypereutectic composition as indicated in Table I. The material was cast in a coupon with circular cross section of the kind used to evaluate the carbon equivalent. A longitudinal mid-plane section of the specimen together with a scheme of the coupon and the thermocouple are shown in Figure 6.

The thermal history was recorded by cooling and cooling rate curves corresponding to the central zone of the part (zone 5 in Figure 6(c)). The metallurgical study encompasses the determination of ferrite phase fraction in five zones of the sample (zones 1 to 5 in Figure 6(c)), and the mean ferrite grain radius in the central zone of the sample (zone 5 in Figure 6(c)).

Due to axial symmetry of the part employed in the cast, only a half of the longitudinal plane was discretized with quadrilateral four-node elements, using 2838 and 525 elements to represent the cast part and the mold, respectively; see Figure 7.

Contact elements were used to simulate the heat flow between the part and the cup, whereas surface elements were considered to deal with the heat extraction through convection in the external surface of the part and the mold in contact with the ambient temperature.

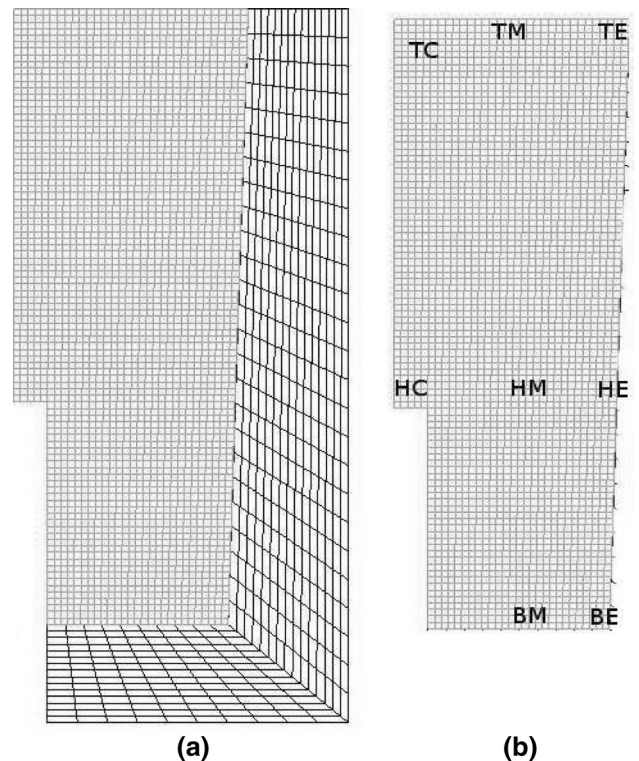


Fig. 7—FE mesh used in the simulations. (a) Axisymmetric FE mesh of the specimen and mold. (b) Location of the nodes where the results are analyzed (Reprinted from Ref. [17]).

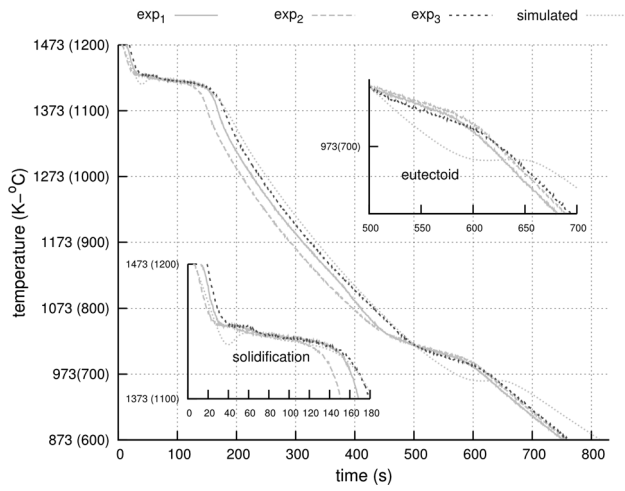


Fig. 8—Comparison of simulated and experimental cooling curves at the central zone of the specimen with magnification of solidification and eutectoid zones [zone 5 in Fig. 6(c) and node HC in Fig. 7(b)] (Reprinted from Ref. [17]).

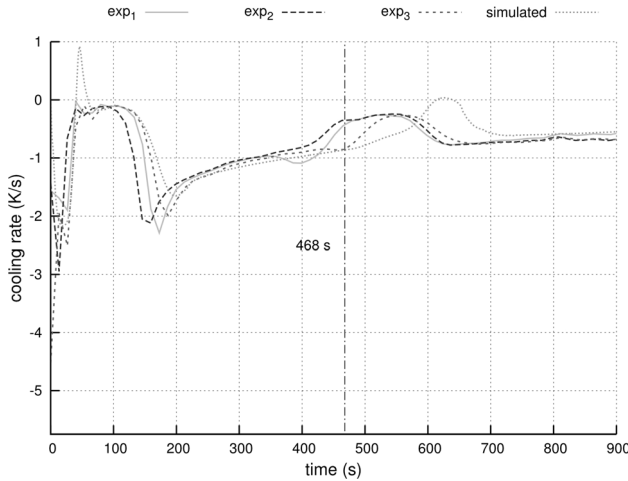


Fig. 9—Comparison of simulated and experimental cooling rate curves at the central zone of the specimen with magnification of solidification and eutectoid zones (zone 5 in Fig. 6(c) and node HC in Fig. 7(b)) (Reprinted from Ref. [17]).

All the thermo-physical properties, material parameters and coefficients and parameters used in the numerical simulations are given in Appendix C.

## V. RESULTS, DISCUSSION, AND EXPERIMENTAL VALIDATION

Computed cooling curves and cooling rate curves at the central region of the sample are next compared with those corresponding to three experiments. The experimental and computed cooling curves and cooling rate curves are shown in Figures 8 and 9, respectively. Two regions are of special interest: solidification between 1473 K and 1373 K (1200 °C and 1100 °C), and eutectoid transformation. The complete graphs showed in Figure 8 show good agreement between the

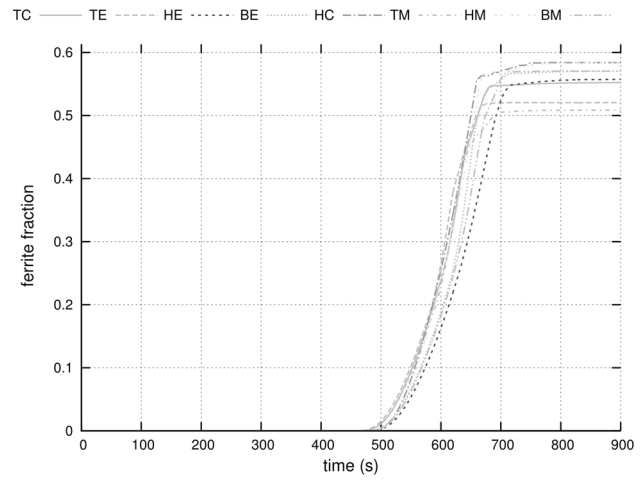


Fig. 10—Volume fraction of ferrite in function of time.

**Table II. Solidification Time ( $t_f$ ), Initiation Time of the Stable Eutectoid Transformation ( $t_x^{ini}$ ), and Cooling Rate Before Solidification Start ( $\dot{T}$ )**

Node	$t_f$ (s)	$t_x^{ini}$ (s)	$\dot{T}$ (K/s)
TE	124	442	-2.6
TM	130	448	-2.5
TC	144	450	-2.47
BE	148	456	-2.92
BM	152	460	-2.66
HE	176	464	-2.2
HM	180	466	-1.76
HC	180	468	-1.72

experimental and compute cooling curves. The largest difference is in the eutectoid region of the graphs. The difference regarding the stable and metastable eutectoid phase changes region in Figures 8 and 9 is the most important. The slope in the eutectoid region in the numerical cooling curve is greater than those in the experimental measurements. The results suggest an underestimation of the latent heat of the stable eutectoid phase change because in the numerical curve, the stable eutectoid transformation starts approximately at the same time as that of the experimental curve (*i.e.*, 468 seconds as shown in Figure 9).

Curves of the evolution of ferrite volume fraction are shown in Figure 10. The results show that nodes located in zones identified as TE and TM in Figure 7(b), for which solidification times were the lowest, are the first to start the eutectoid transformation. This is also shown in the results of Table II. The other curves show similar start times for the eutectoid transformation. The differences in ferrite volume fractions between different zones is negligible, with 8 pct difference between the maximum and minimum ferrite fractions, which is almost 13 pct of the maximum ferrite volume fraction.

Figure 11 shows the time elapsed between the initiation of the eutectoid stable and metastable transformations for eight zones considered in the computational analysis. From Figures 10 and 11, it may be seen that



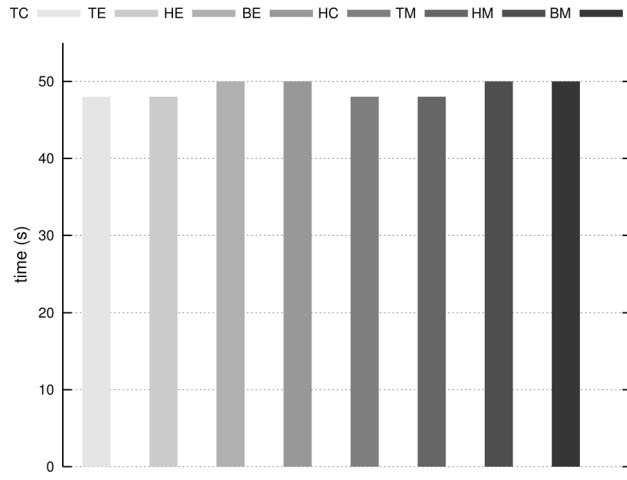


Fig. 11—Computed elapsed time from the start of the stable eutectoid transformation until the beginning of metastable eutectoid transformation.

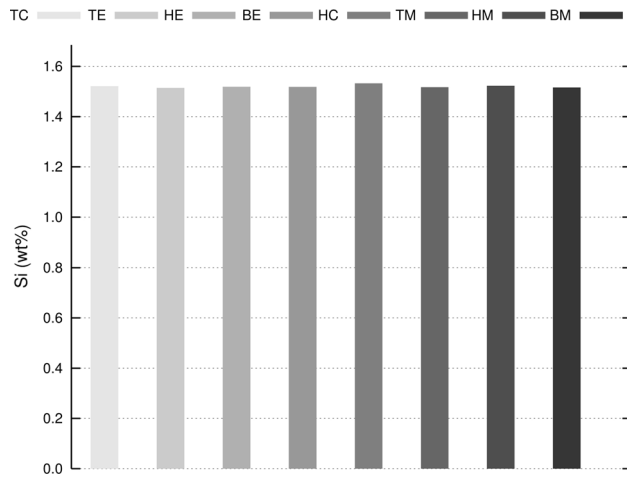


Fig. 12—Computed concentrations of silicon at the end of solidification.

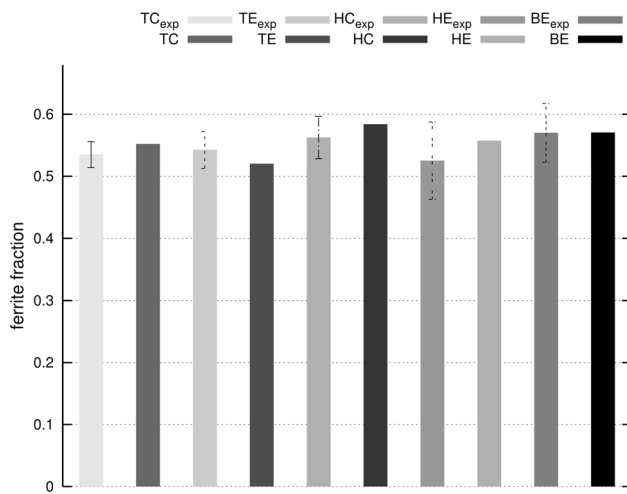


Fig. 13—Experimental ferrite fraction (per unit area) at the five points shown in Fig. 6(c) and simulated ferrite fraction (per unit volume) at the nodes TC, TE, HC, HE, and BE indicated in Fig. 7(b).

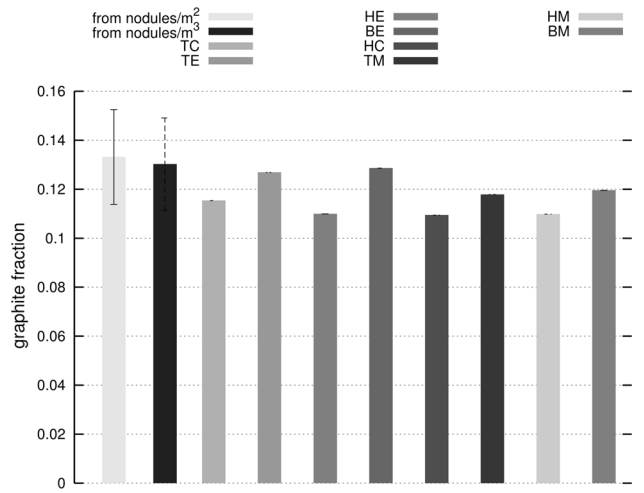


Fig. 14—Experimental (at point 5 in Fig. 6(c)) and simulated graphite fraction (Reprinted from Ref. [17]).

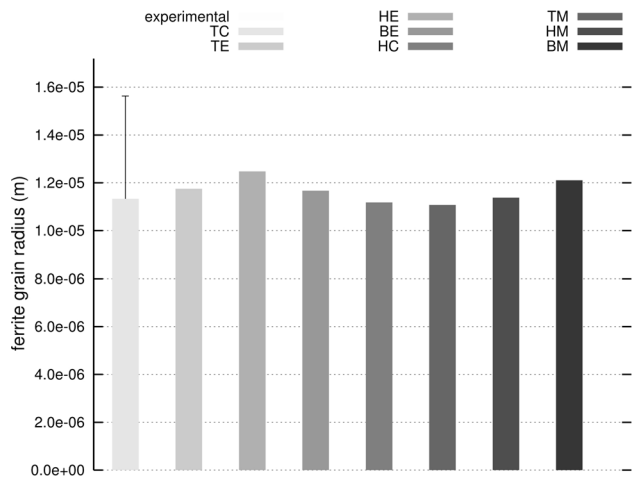


Fig. 15—Experimental [at point 5 in Fig. 6(c)] and simulated average 2D view of ferrite grain radius.

there is a relation between the final values of ferrite volume fraction and the time from the beginning of stable and metastable eutectoid transformations. This suggests that there is a conditioning effect on the initiation of metastable eutectoid transformation in the development of the stable eutectoid transformation, on the competitive nature of stable and metastable eutectoid transformations, and on the slight trend in the curves to be stratified depending on their characteristics. This may be seen in the three nodes located at the top of the finite element mesh (TC, TM, and TE in Figure 7(b)), which have the lowest ferrite fractions; the nodes located at the bottom region (BM and BE) have intermediate values of ferrite fractions, and finally, those located at the middle (HC, HM, and HE) have larger values.

In the evaluation of the ferrite fraction, there are other factors that should be taken into account: the time of transformation and of the initiation of the stable eutectoid transformation, and the number of potential sites for the nucleation of ferrite grains, with the variables taking into account in this article, *e.g.*,

thermodynamics values corresponding to temperatures and equilibrium carbon concentration, critical temperatures, equilibrium carbon concentrations at interphases, numbers of initial grains nucleated at graphite/austenite interphase and different laws of ferrite grain growth in function of the temperature and size, and numbers of graphite and ferrite grains.

Values of weight concentrations of Si at the end of the solidification process are represented in Figure 12 for different zones in the considered coupon, and the results show great similarities of concentrations in the zones considered. This leads to similar temperatures for the initiation of a metastable eutectoid transformation because the model postulates that pearlite colonies nucleate in the last zones that become solid,<sup>[18]</sup> which in turn correspond to values of Si concentration as indicated in Figure 12.

The capability of taking Si concentration into account is of importance in parts with different quantities of Si due to nonequilibrium solidification (microsegregation). The reason is that the Si concentration plays a crucial role in the temperature difference between upper bounds of intercriticals stable and metastable eutectoid ranges.

Figure 13 shows ferrite fractions from experiments in five points of the coupon indicated in Figure 6(c), which are compared with computational results for equivalent zones showed in Figure 7(b) (TC, TE, HE, BE and HC). On other hand, in the experiments, the difference between the maximum and minimum ferrite fractions was of 8 pct, whereas 11 pct was obtained from the computations; further, the differences are within the expected standard deviation of the experimental results with respect to their mean value.

Figure 14 shows graphite fractions from nodules per area and volume at point 5 in Figure 6(c), which are compared with computational simulations for eight zones indicated in Figure 7(b). All numerical values are within the expected standard deviation of the experiments with respect to the mean value.

The radii of ferrite grains are shown in Figure 15; these are equivalent to the thickness of ferrite shells which may or may not fully surround the spheroids. In the experiments, 50 measurements of 2D view of ferrite grains were made in a micrograph of the central region. Computational results are found to be within the standard deviation of the experiments and very close to the mean value.

## VI. CONCLUSIONS

A new model to simulate the stable eutectoid transformation of spheroidal cast irons, which is coupled with a microstructural model of solidification, graphite growth, and metastable eutectoid transformation has been presented in this paper. A number of original contributions have been incorporated in the model: (i) The effects of carbon quantity in austenite at the beginning of the transformation; (ii) The influence of Si on the temperature of the initiation of the metastable eutectoid transformation; and (iii) The fraction of transformed ferrite during and after the intercritical stable eutectoid range.

The main conclusions of the study may be summarized as follows:

1. The model presented in this article can explain the changes that occur during the intercritical stable eutectoid. This is very important for designing processes and heat treatments that include the transformation of austenite during the intercritical stable eutectoid.
2. Predictions of this model are in general agreement with those obtained by other authors, in the sense that ferrite fractions increase at nodes having more graphite spheroids, higher local times of solidification, and higher time intervals between the initiation of stable and metastable eutectoid transformations.
3. From the results, it was found that there is a relation between the time interval from the beginning of the stable and metastable eutectoid transformation, and the values of ferrite fraction at the end of the cooling process.

## ACKNOWLEDGMENTS

The authors thank the contribution of Prof. Jacques Lacaze in obtaining the equations reported in Appendix A. The company Sánchez and Piccioni allowed using its facilities to carry out the casts. Fernando D. Carazo and Luis A. Godoy are members of the research staff of CONICET. Diego J. Celentano thanks to CONICYT (Chilean Council of Research and Technology) for the support provided by Project Fondecyt 1130404.

## APPENDIX A: PHASE DIAGRAMS

The equilibrium carbon concentrations for eutectoid phase changes together with the lower and upper bounds of the intercriticals stable and metastable eutectoid ranges in the Fe-C-Si and Fe-Fe<sub>3</sub>C-Si systems are

Fe-C-Si:

$$C_C^{\beta/\delta} = 1.60 \times 10^{-3} + 8.13 \times 10^{-5} C_{Si} - 6.46 \times 10^{-6} T \\ + 5.47 \times 10^{-6} (C_{Si})^2 + 1.85 \times 10^{-8} T^2 - 1.05 \times 10^{-4} C_{Si} T,$$

$$C_C^{\alpha/\beta} = -9.53 \times 10^{-4} + 1.02 \times 10^{-2} C_{Si} + 1.55 \times 10^{-6} T \\ + 9.59 \times 10^{-4} (C_{Si})^2 + 1 \times 10^{-10} T^2 - 1.76 \times 10^{-5} C_{Si} T,$$

$$C_C^{\gamma/\delta} = 1.92 \times 10^{-3} - 1.59 \times 10^{-2} C_{Si} - 4.12 \times 10^{-6} T \\ - 2.62 \times 10^{-3} (C_{Si})^2 + 2.31 \times 10^{-9} T^2 + 2.5 \times 10^{-5} C_{Si} T,$$

$$C_C^{\gamma/\alpha} = 1.29 \times 10^{-1} + 5.13 \times 10^{-3} C_{Si} - 2.56 \times 10^{-4} T + 2.9 \\ \times 10^{-4} (C_{Si})^2 + 1.24 \times 10^{-7} T^2 + 3.27 \times 10^{-4} C_{Si} T,$$

**Table C3. Thermo-Physical Properties and Material Parameters of Cast Iron**

Temperature [K (°C)]	Thermal Conductivity (W/mK)		Specific Heat (J/kg)	
	Conductivity		Temperature [K (°C)]	$C_p$
553 (280)	54.1		293 (20)	$500 \times 10^3$
693 (420)	38.1		873 (600)	$750 \times 10^3$
833 (560)	47.1		1073 (800)	$750 \times 10^3$
973 (700)	43.6		1418 (1145)	$820 \times 10^3$
1113 (840)	38.1		1428 (1155)	$840 \times 10^3$
1253 (980)	32.5		1673 (1400)	$840 \times 10^3$
1393 (1120)	28.8			
1673 (1400)	45			
Mass density (kg/m <sup>3</sup> )	7300			
Solidification phase change model <sup>[19]</sup>				
Eutectic latent heat	(J/kg)		$2 \times 10^5$	
Carbon diffusion coefficient in liquid and austenite	(m <sup>2</sup> /s)		$D_C^L = 5 \times 10^{-10}$ and $D_C^A$ <sup>[10]</sup>	
Graphite nucleation coefficients	$b^M = 1 \times 10^{13}$ (grains/m <sup>3</sup> Ks)		$c^M = 280$ (K)	
Graphite initial radius	(m)		$R_g^0 = 5.0 \times 10^{-7}$	
Austenite nucleation coefficient	(grains s/m <sup>3</sup> K)		$A_\gamma = 1 \times 10^{-7}$	
Gibbs-Thompson coefficient	(K $\mu$ m)		$\Gamma_{GT} = 2 \times 10^{-7}$	
Graphite and austenite densities	(kg/m <sup>3</sup> )		$\rho_g = 2023$ and $\rho_\gamma = 7000$	
Solid state phase change model <sup>[18]</sup>				
Initial thickness of the boundary layer ahead of the front of transformation (m)	$\delta = 5 \times 10^{-10}$ <sup>[20]</sup>			
Ferrite latent heat	(J/kg)		$6 \times 10^4$	
Initial numbers of ferrite grains	(grains)		$n_z = 9$	
Initial radius of ferrite grains	(m)		$R_z^0 = 1 \times 10^{-8}$	
Pearlite latent heat	(J/kg)		$9 \times 10^4$	
Pearlite nucleation coefficient	(grains s/m <sup>3</sup> K)		$\mu_P = 1 \times 10^{10}$	
Carbon diffusion coefficient in austenite and austenite/pearlite interface	(m <sup>2</sup> /s)		$D_C^A$ <sup>[10]</sup> and $D_C^B$ <sup>[21]</sup>	
Enthalpy change during austenite-pearlite transformation	(J/kg)		$\Delta H_V^P$ <sup>[21]</sup>	
Interfacial free energy in ferrite at interface with cementite	(J/m <sup>2</sup> )		$\sigma^{\alpha/\theta}$ <sup>[22]</sup>	

**Table C4. Thermo-Physical Properties of Sand**

Temperature [K (°C)]	Thermal Conductivity (W/mK)
373 (100)	0.54
573 (300)	0.57
773 (500)	0.65
973 (700)	0.79
1173 (900)	1.00
1373 (1100)	1.26
1573 (1300)	1.59
1673 (1400)	1.59
Mass density (kg/m <sup>3</sup> )	1550
Specific heat (J/kg)	$1 \times 10^6$

**Table C5. Specimen-Mold Conductance Coefficient**

Temperature [K (°C)]	Conductance Coefficient (W/m <sup>2</sup> K)
293 (20)	60
773 (500)	70
1123 (850)	90
1443 (1170)	100
1673 (1400)	100

**Table C6. Specimen-Environment and Mold-Environment Convection Heat Transfer Coefficients**

Temperature [K (°C)]	Heat Transfer Coefficient (W/m <sup>2</sup> K)
293 (20)	50
1673 (1400)	80

**Table C7. Specimen-Termocouple Conductance Coefficient**

Interface	Heat Transfer Coefficient (W/m <sup>2</sup> K)
Part-termocouple	40

$$T_{ar}^\alpha = - \left( \sqrt{1.10 \times 10^{11}} \sqrt{2.74 \times 10^{35} (C_{Si})^2 - 3.25 \times 10^{35} C_{Si} + 1.46 \times 10^{34}} + 1.74 \times 10^{23} C_{Si} - 1.02 \times 10^{23} \right) / 8.53 \times 10^{19},$$

$$T_{A_1}^{\alpha} = - \left( \sqrt{3.47 \times 10^{11}} \right. \\ \left. \sqrt{1.60 \times 10^{22}(C_{Si})^2 - 2.19 \times 10^{21}C_{Si} + 5.85 \times 10^{19}} \right. \\ \left. + 7.4 \times 10^{16}C_{Si} - 9.85 \times 10^{15} \right) / 7.69 \times 10^{12}.$$

Fe-Fe<sub>3</sub>C-Si:

$$C_C^{\alpha/0} = -7.34 \times 10^{-3} + 1.82 \times 10^{-1}C_{Si} + 1.7 \times 10^{-6}T + 2.92 \\ \times 10^{-2}(C_{Si})^2 + 1.72 \times 10^{-8}T^2 + 4.17 \times 10^{-5}C_{Si}T,$$

$$C_C^{\alpha/0} = 2.99 \times 10^{-3} + 1.37 \times 10^{-4}C_{Si} - 9.84 \times 10^{-6}T + 1.10 \\ \times 10^{-5}(C_{Si})^2 + 8.23 \times 10^{-9}T^2 - 1.89 \times 10^{-6}C_{Si}T,$$

$$T_{at}^P = - \left( \sqrt{2.16 \times 10^{10}} \right. \\ \left. \sqrt{5.07 \times 10^{20}(C_{Si})^2 - 3.94 \times 10^{20}C_{Si} + 5.23 \times 10^{19}} \right. \\ \left. + 3.08 \times 10^{15}C_{Si} - 2.82 \times 10^{15} \right) / 2.32 \times 10^{12},$$

$$T_{A_1}^P = - \left( \sqrt{4.05 \times 10^{11}} \right. \\ \left. \sqrt{6.72 \times 10^{21}(C_{Si})^2 - 7.3 \times 10^{20}C_{Si} + 7.5 \times 10^{19}} \right. \\ \left. + 5.46 \times 10^{16}C_{Si} + 1.16 \times 10^{16} \right) / 2.4 \times 10^{13},$$

where  $C_{Si}$  is the Si content in austenite at different interfaces expressed in weight percentage and  $T$  is the temperature of the alloy in Celsius degrees.

## APPENDIX B: COMPUTATION OF CARBON QUANTITY IN AUSTENITE, SURFACE OF NODULES IN CONTACT WITH FERRITE AND AUSTENITE

The value of  $C_C^{\gamma}$ , used in Eqs. [5], [6], [11] per unit volume of RVE is computed as<sup>[17]</sup>

$${}^{t+\Delta t}C_C^{\gamma} = \frac{{}^tC_C^{\gamma}\rho_{\gamma}(1 - {}^tU_g - {}^tU_x - {}^tU_P) + C_g\rho_g({}^tU_g - {}^{t+\Delta t}U_g) + C_{\alpha c}\rho_{\alpha}({}^tU_x - {}^{t+\Delta t}U_x) + C_{Pc}\rho_P({}^tU_P - {}^{t+\Delta t}U_P)}{\rho_{\gamma}(1 - {}^{t+\Delta t}U_g - {}^{t+\Delta t}U_x - {}^{t+\Delta t}U_P)}, \quad [B1]$$

where  $C_{Xc}$ ,  $\rho_X$ , and  ${}^tU_X$  are carbon concentrations in weight percentage, density, and carbon quantity in a microconstituent X, respectively. X may be austenite, graphite, ferrite, or pearlite. The derivation of Eq. [B1] may be seen in Reference 18.

The fraction of the j-th nodule surface in contact with austenite (present in Eq. [6]) in contact with ferrite and austenite, are given as fractions as

$$A_{\alpha/g_j} = \frac{\sum_{i=1}^{n_f} (R_{\alpha_i})^2}{4(R_{g_j})^2}, \quad [B2] \\ A_{\gamma/g_j} = 1 - A_{\alpha/g_j},$$

where  $n_f$  is the number of ferrite grains nucleated on each graphite spheroid (see Table C3) and  $R_{\alpha_i}$  is the radius of ferrite grains nucleated on the spheroid.

## APPENDIX C: THERMO-PHYSICAL PROPERTIES AND MATERIAL PARAMETERS USED IN THE NUMERICAL SIMULATIONS

Tables C3 and C4 show the values of coefficients and thermo-physical properties of the alloy and sand used in the numerical simulation. Tables C5 through C7 show the conductance and heat transfer coefficients at different materials interfaces. The initial temperature of alloy is the same as the maximum value recorded in the experiments: 1478 K (1205 °C). The initial temperature for the cylindrical cup is the environment at the moment of conducting the experiments: 293 K (20 °C).

## REFERENCES

1. ASTM A247-10, *ASTM International*, West Conshohocken, 2010. DOI:10.1520/A0247-10.
2. ASTM A536-84, *ASTM International*, West Conshohocken, 2014. DOI: 10.1520/A0536-84R14.
3. A.I. Al-Ghonamy, M. Ramadan, N. Fathy, K.M. Hafez, and A.A. El-Wakil: *IJCEE-IJENS*, 2010, vol. 10 (3), pp. 1–4.
4. A. Basso, R. Martinez, and J. Sikora: *J. Alloys Compd.*, 2011, vol. 509 (41), pp. 9884–89.
5. D.M. Stefanescu and C.S. Kanetkar: in *Computer Simulation of Microstructural Evolution*, D.J. Srolovitz, ed., TMS, Warrendale, 1985, pp. 171–88.
6. B.C. Liu, H.D. Zhao, W.Y. Liu, and D.T. Wang: *Int. J. Cast Met. Res.*, 1999, vol. 11 (5), pp. 471–76.
7. S. Chang, D. Shangquan, and D.M. Stefanescu: *Metall. Trans. A*, 1992, vol. 23A (4), pp. 1333–46.
8. A. Almansour, K. Matsugi, T. Hatayama, and O. Yanagisawa: *Mater. Trans. JIM*, 1996, vol. 37 (4), pp. 612–19.

9. M. Wessen and I.L. Svensson: *Metall. Trans. A*, 1996, vol. 27A, pp. 2209–20.
10. J. Lacaze and V. Gerval: *ISIJ Int.*, 1998, vol. 38 (7), pp. 714–22.
11. D. Venugopalan: in *The Physical Metallurgy of Cast Iron. Proceedings of the Fourth International Symposium on the Physical Metallurgy of Cast Iron*, G. Ohira, T. Kusakawa, E. Niyama,



- eds., Materials Research Society, Tokyo, Japan, 1989, pp. 271–78.
12. D. Venugopalan: *Metall. Trans. A*, 1990, vol. 21A, pp. 913–18.
  13. F.D. Carazo, P.M. Dardati, D.J. Celentano, and L.A. Godoy: *Metall. Trans. B*, 2012, vol. 43 (6), pp. 1579–95, DOI:[10.1007/s11663-012-9710-y](https://doi.org/10.1007/s11663-012-9710-y).
  14. A. Fick: *Ann. Phys. (Berlin, Ger.)*, 1855, vol. 170 (1), pp. 59–86.
  15. P.G. Shewmon: *Diffusion in Solids*, 2nd ed., Wiley, New York, 1989, p. 28.
  16. W. Kurz and D.J. Fisher: *Fundamentals of Solidification*, 1st ed., TransTech Public, Stafa-Zurich, 1984, p. 98.
  17. F.D. Carazo, P.M. Dardati, D.J. Celentano, and L.A. Godoy: *Metall. Trans. A*, 2016, vol. 47 (6), pp. 2625–41, DOI:[10.1007/s11661-016-3430-x](https://doi.org/10.1007/s11661-016-3430-x).
  18. F. D. Carazo: Ph.D. Thesis, Facultad de Ciencias Exactas Físicas y Naturales, Universidad Nacional de Córdoba, 2012.
  19. P. M. Dardati: Ph.D. Thesis, Facultad de Ciencias Exactas Físicas y Naturales, Universidad Nacional de Córdoba, 2005.
  20. D.M. Stefanescu: *Science and Engineering of Casting Solidification*, 2nd ed., Springer, New York, 2009, p. 21.
  21. A. S. Pandit: Ph.D. Thesis, Department of Materials Science and Metallurgy, University of Cambridge, 2011.
  22. J.J. Kramer, G.M. Pound, and R.F. Mehl: *Acta Metall.*, 1958, vol. 6 (12), pp. 763–771.